



An Electrochemical Approach to Prepare Liquid Sodium-Lead Alloy using a Molten NaCl–Na₂CO₃ Electrolyte

YONGXIN WU, HONGYA WANG, MENGLI XIANG, ZUOJUN HU, HAO SHI,
FANGZHAO PANG, BINGBING WANG, XIONG ZHANG, DIHUA WANG,
XIAOWEI LIU, and HUAYI YIN

Alloying alkaline metals (AMs) and/or alkaline-earth metals (AEMs) with lead (Pb) is an effective way to increase the mechanical strength of Pb alloys that are commonly employed as grids of lead-acid batteries (LABs). However, current methods for making AM/AEM-Pb alloys by physically mixing pure AM/AEM and Pb face challenges such as instantaneous thermal runaway from exothermic alloy reactions and oxidation of AM/AEM. Herein, sodium-lead (Na–Pb) alloy is directly prepared by molten salt electrolysis without generating Cl₂ gas using a molten NaCl–Na₂CO₃ electrolyte with a current efficiency of above 80 pct at 200 mA·cm⁻², because the discharge of CO₃²⁻ is significantly more favorable than that of Cl⁻ at the graphite anode. Furthermore, the reduction of Na⁺ on the liquid Pb electrode happens at a potential more positive than the reduction of pure Na. The diffusion coefficient of Na in liquid Pb is measured as 3.22×10^{-4} cm² s⁻¹ at 750 °C by the galvanostatic intermittent titration technique (GITT), and the simulated electrolysis current density is 200 mA cm⁻². Moreover, the prepared Pb–Ca–Na–Al using the electrolytic Na–Pb alloys achieves a significant mechanical strength improvement (27 pct increase of the hardness, 60 pct increase of the creep resistance). Overall, molten salt electrolysis offers a clean and efficient method for preparing various Pb alloys for next-generation LABs and other applications.

<https://doi.org/10.1007/s11663-025-03596-7>

© The Minerals, Metals & Materials Society and ASM International 2025

I. INTRODUCTION

BATTERIES play an increasingly important role in the electrification of our society.^[1–5] Among many types of batteries, lead-acid batteries (LABs) that were invented in 1859, are still commonly used in our daily life such as electric motorcycles, automotive start-stop systems, and energy storage applications.^[6–9] By 2024, global sales of LABs are expected to reach \$28 billion.^[10] Historically, lead (Pb) grids have been used to hold the Pb paste because they can increase the energy density of LABs.^[9,11] However, Pb is too soft to maintain the integrity of the paste electrode under varying operating conditions.^[12] Thus, adding small amounts of calcium (Ca) is effective in increasing the mechanical strength of Pb grids.^[13–15] According to the principle of strength improvement, adding other AMs and/or AEMs should be possible to achieve similar efficacy because AM/AEMs and Pb can form high-melting point intermetallics.^[16,17] However, directly mixing AM/AEMs and Pb will generate lots of heat because of their big differences of electronegativity, which is the

YONGXIN WU is with the School of Resource and Environmental Science, Wuhan University, 299 Bayi Road, Wuchang District, Wuhan 430072, P. R. China and also with the Joint Center of Green Manufacturing of Energy Storage Materials of Wuhan University and Chilwee, Wuhan 430072, P. R. China. HONGYA WANG, ZUOJUN HU, HAO SHI, and FANGZHAO PANG are with the School of Resource and Environmental Science, Wuhan University. MENGLI XIANG, BINGBING WANG, XIONG ZHANG, and XIAOWEI LIU are with the Joint Center of Green Manufacturing of Energy Storage Materials of Wuhan University and Chilwee Contact email: liuxw888@126.com. DIHUA WANG and HUAYI YIN are with the School of Resource and Environmental Science, Wuhan University and with the Joint Center of Green Manufacturing of Energy Storage Materials of Wuhan University and Chilwee and also with the Hubei International Scientific and Technological Cooperation Base of Sustainable Resource and Energy, Wuhan University, Wuhan 430072, P. R. China. Contact email: yinhuayi@whu.edu.cn

Manuscript submitted December 23, 2024; accepted May 7, 2025.

Article published online June 4, 2025.

same theory of liquid metal batteries.^[18–21] Therefore, it is necessary to develop different ways to prepare AM/AEM-Pb alloys without using pure active metals.

In addition to Ca, Na is also a promising alloying element to increase the mechanical strength of Pb alloys because there are many types of Na–Pb intermetallic alloys according to the phase diagram.^[22–24] There may exist NaPb_3 , NaPb , Na_3Pb_2 , $\text{Na}_{15}\text{Pb}_4$ and Na_4Pb , when increasing the concentration of Na in Pb. Industrially, Na is extracted by molten salt electrolysis (MSE) of $\text{NaCl}-\text{CaCl}_2$, also named the *Downs' process*.^[25] However, the commercial production of Na–Pb alloy is still absent. There could be several reasons: (1) the reactivity of Na is too high,^[26] (2) the density disparity of Na and Pb is large, and (3) the production of Na will generate Cl_2 gas.^[27] These reasons will lead to the safety issues related to the thermal runaway and explosion caused by the alloying reaction,^[28] high-Na loss rate because of the oxidation, inhomogeneousness related to the large density difference, and the difficult management of Cl_2 gas for the production of AEMs by molten salt electrolysis.^[29,30] The preparation of M–Pb (M:Eu,^[31] Ti,^[32] Ca,^[13,33] Na,^[33,34] etc.) in molten chloride has been tried, but it still generates Cl_2 . Thus, engineering the electrolyte has been proven as an effective way to generate Na–Sn without the generation of Cl_2 .^[35–37] Thus, the preparation of liquid Na–Pb in molten $\text{NaCl}-\text{Na}_2\text{CO}_3$ could be a promising way to control the alloying rate and thereby avoid instantaneous heat generation, the oxidation of Na, and Cl_2 generation.

In this study, we propose a process for directly preparing Na–Pb master alloys through molten salt electrolysis in an electrolyzer containing a liquid Pb cathode, a molten $\text{NaCl}-\text{Na}_2\text{CO}_3$ electrolyte, and a graphite anode at 750 °C at different current densities. Thermodynamic analysis was conducted to predict the deposition of Na^+ and CO_3^{2-} ions in the liquid Pb electrode, as well as the oxidation of CO_3^{2-} and Cl^- ions at the carbon anode. In addition, the diffusion coefficient of Na in the liquid Pb electrode was studied using galvanostatic intermittent titration technique (GITT), along with diffusion simulation studies. Ultimately, pilot-scale production of Na–Pb master alloy was achieved in a 100-A-scale electrolysis cell. The produced master alloy was used to prepare grid alloys, and the mechanical properties of these grid alloys were measured.

II. MATERIALS AND METHODS

A. Materials

Anhydrous NaCl (analytical reagent (AR), 99.9 pct), Na_2CO_3 (AR, 99.9 pct), Na (AR 99.7 pct), and AgCl (AR 99.9 pct) used in this work were purchased from Aladdin Bio-Chem Technology (Shanghai, China). NaCl and Na_2CO_3 were vacuum-dried at 250 °C for 10 hours before use. Pb (99.99 pct) was purchased from Chilwee Power (Zhejiang, China). Molybdenum (Mo) wire was purchased from Bilong Metal Materials (Shanxi, China). The purity of argon (Ar) is 99.99 pct.

Graphite rods and crucibles (spectrum purity, 99.9 pct) were purchased from Sino Steel Group Shanghai Advanced Graphite Materials (Shanghai, China). Alumina tubes & crucibles and mullite tubes & crucibles were purchased from Changsha Miqi Instrument (Hunan, China).

B. Preparation of Liquid Na–Pb Alloy by Molten Salt Electrolysis

Two-electrode electrolysis was conducted in molten $\text{NaCl}-\text{Na}_2\text{CO}_3$. Initially, 500 g of pre-dried NaCl and Na_2CO_3 (molar ratio: 57.7:42.3) were uniformly mixed. Then, the dried electrolyte was then transferred to a stainless-steel (SS) reactor heated by a resistance furnace. Under an Ar atmosphere, the temperature was raised to 750 °C at a rate of 5 °C min⁻¹. Third, a pre-electrolysis was performed for 1 hour at 200 mA between a liquid Pb cathode (area: 5.5125 cm⁻²) and a graphite anode (diameter: 10 mm) to remove impurities and moisture. Using a computer-controlled Neware DC power supply (Guangdong, China), Na–Pb alloys with theoretical Na compositions of 0.5, 1.0, 1.5, 2.0, and 3.0 wt pct were prepared at a current density of 200 mA cm⁻² by varying electrolysis times. Additionally, Na–Pb alloys with a 2.0 wt pct Na content were produced under different current densities (50 mA cm⁻², 100 mA cm⁻², 200 mA cm⁻², 300 mA cm⁻², and 500 mA cm⁻²), respectively.

The electrolysis time was calculated based on the Faraday's law, while the current efficiency was determined by the actual Na content measured in the liquid Pb electrode compared to the theoretical Na content (Eq. 1).

$$\eta_{\text{Current efficiency}} = \frac{Q_{\text{theoretic}}}{Q_{\text{actual}}} \times 100 \text{ pct}, \quad [1]$$

where the $Q_{\text{theoretic}}$ was calculated based on the required charge (C) of Pb obtained from the cathode, and the Q_{actual} was recorded by the battery testing system.

C. Electrochemical Measurements

The chemical diffusion coefficient of Na in the liquid Pb electrode was determined using a Galvanostatic Intermittent Titration Technique (GITT), as shown in Figure 1. In the GITT measurements, Na–Pb alloys, Ag/ AgCl electrodes, and $\text{Na}_{30}\text{Pb}_{70}$ alloys served as the working electrode (WE), reference electrode (RE), and counter electrode (CE), respectively. The Na–Pb alloy WEs and $\text{Na}_{30}\text{Pb}_{70}$ alloy CEs were prepared using a custom high-frequency induction heating device (Kejing Material Technology, Anhui, China) installed in a glovebox (O_2 , $\text{H}_2\text{O} < 0.01$ ppm). The Na–Pb alloy electrodes were made from pure Na and Pb. The Ag/ AgCl electrode was fabricated by thoroughly mixing anhydrous $\text{Na}_2\text{CO}_3-\text{NaCl}-\text{AgCl}$ in a molar ratio of 42.5:52.5:5.0, followed by vacuum drying for 12 hours. This mixture was then heated to 700 °C and maintained for 30 minutes until melted in the glovebox using the induction heating device and an Al_2O_3 crucible. Once

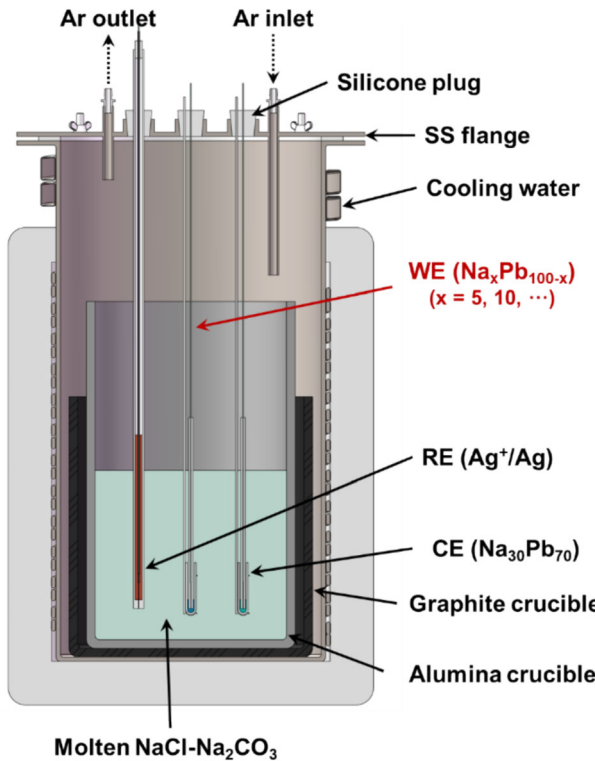


Fig. 1—Schematic diagram of the three-electrode cell apparatus for electrochemical measurements.

the Na_2CO_3 – NaCl – AgCl mixture solidified and cooled to room temperature, 1 g of the powder was packed into a mullite tube (open at one end) with a silver wire (diameter: 1.5 mm) as the current lead. The open end of the mullite tube was sealed with high-temperature adhesive (Sinwe New Materials, Guangdong, China), allowing the silver wire to protrude, forming the Ag/AgCl reference electrode. All alloys, along with a Mo wire (protected by an Al_2O_3 tube), were placed in an Al_2O_3 crucible (inside diameter: 9.0 mm, height: 15.0 mm). In an Ar atmosphere at 750 °C, constant current pulses were applied to the Na – Pb electrode with sodium atomic concentration of 5, 10, 15, and 20 pct.

D. Mechanical Properties of Pb Grid Alloys

Pure Pb, Pb–Ca–Al alloy, and Na – Pb alloy were mixed in proportion to prepare the Pb–Ca– Na –Al alloy, which was then cast into the billets (500 mm × 330 mm × 14 mm). After rolling, the billets were cut and processed into Pb strips (90 mm × 10 mm × 0.7 mm). The resulting samples were heat-treated at 80 °C for 12 hours to obtain age-hardened alloys for mechanical property testing. The alloy hardness was measured using a Portable Hardness Tester (Tianxing Test Instrument Co., Ltd., Shenyang, China). The alloy creep resistance was measured using a universal testing machine (MTS Systems Co. Ltd., Shanghai, China) under a constant low speed of 0.334 mm min^{-1} .

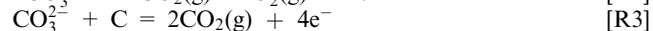
E. Materials Characterization

The crystal structure of the electrolytic Na – Pb alloy was analyzed using X-ray diffraction (XRD, D8 ADVANCE, Bruker, with Cu K_{α} radiation at $\lambda = 1.5405 \text{ \AA}$). The composition and morphology of the electrolytic Na – Pb alloy samples were characterized using scanning electron microscopy (SEM-EDS, FEI Sirion field emission) and energy-dispersive X-ray spectroscopy (EDS, XFlash Detector 5010, Bruker). The concentrations of Pb and Na elements were measured using inductively coupled plasma optical emission spectroscopy (ICP-OES, ICP-5000, Focused Photonics Inc.). The mechanical properties of the Na – Pb alloy were characterized using an electromechanical universal testing machine (CMT6503, 5-5000N) equipped with a hydraulic system and force sensor.

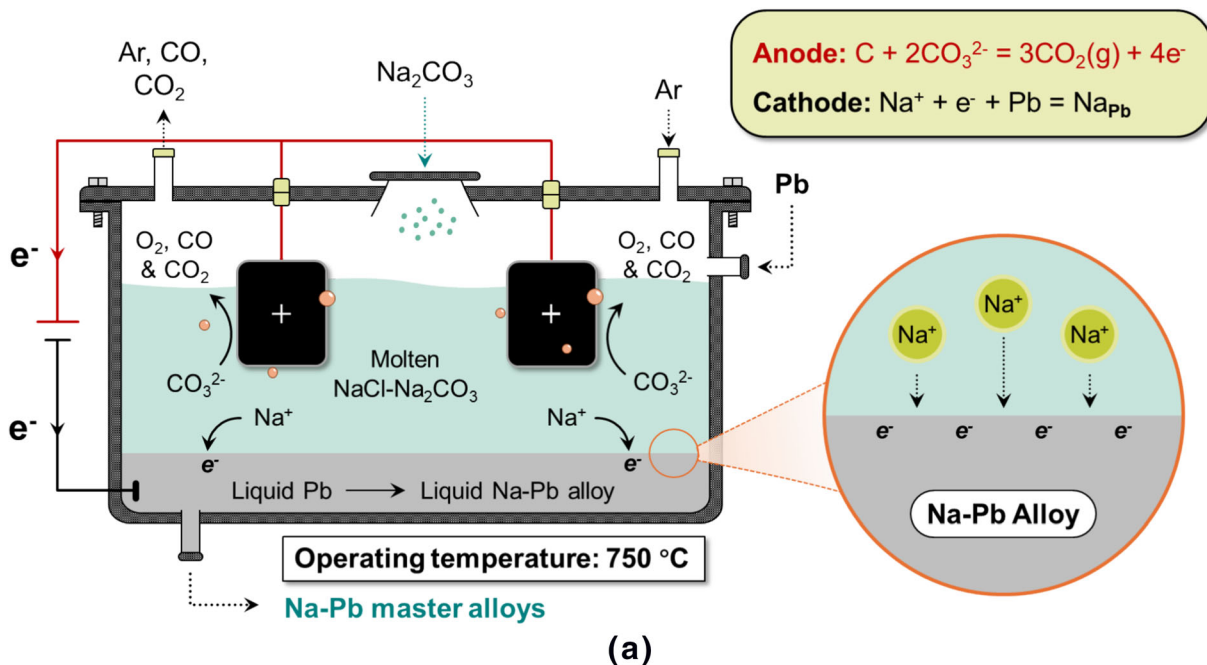
III. RESULTS AND DISCUSSION

A. Electrochemical Preparation of Liquid Na – Pb Alloy

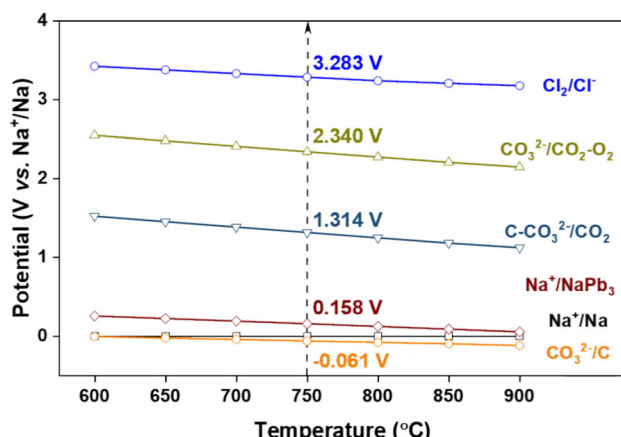
A liquid Pb cathode and a graphite anode were used to prepare Na – Pb alloys in molten NaCl – Na_2CO_3 at 750 °C. A schematic diagram of this process is shown in Figure 2(a). The possible reactions occurring in this system are as follows:



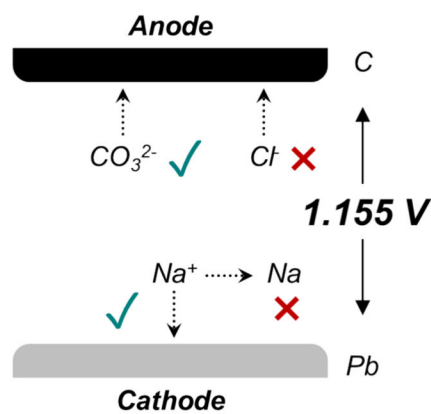
According to the theoretical reaction potentials [Figure 1(b)], the thermodynamic potential for the generation of CO_2 and O_2 at an inert anode is 2.34 V (vs. Na^+/Na) (R2), which is 0.943 V lower than the potential for the evolution of Cl_2 (R1). This means that the discharge of CO_3^{2-} is more favorable than Cl^- . In the cathode region, the thermodynamic potential for the formation of NaPb_3 alloy is approximately 0.16 V (vs. Na^+/Na), indicating that the formation of NaPb_3 is thermodynamically more favorable than the formation of Na (R4–R5). For the reduction of CO_3^{2-} to C (R6), the potential is 0.219 V lower than the formation potential of NaPb_3 , meaning that the formation of NaPb_3 is easier than the formation of pure Na and C.^[38] At the anode side, the formation potential of $\text{CO}_2(\text{g})$ is 1.969 V lower than the generation of Cl_2 using graphite, meaning that $\text{CO}_2(\text{g})$ is a thermodynamically favorable anodic product at a graphite anode [Figure 1(c)].^[39] Therefore, Na_2CO_3 prevents the generation of Cl_2 , while NaCl is used to lower the melting point of the salt and reduce energy consumption. The use of liquid Pb as the cathode facilitates the alloying of metallic Na with Pb, thereby minimizing Na dissolution and loss in the molten salt.^[40]



(a)



(b)

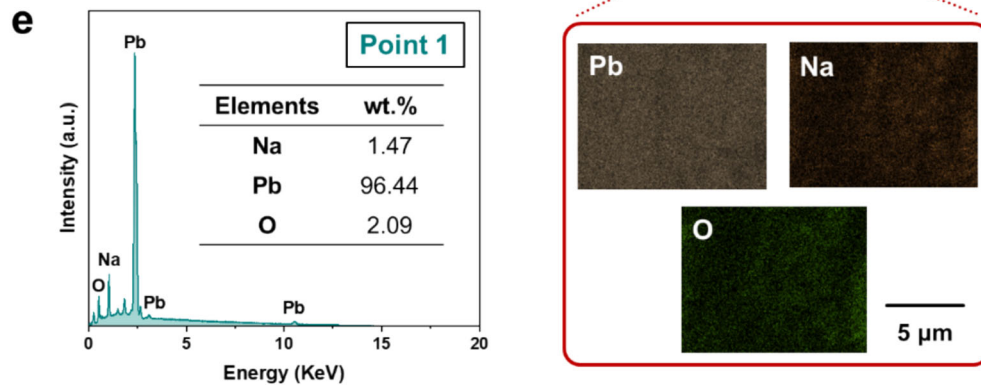
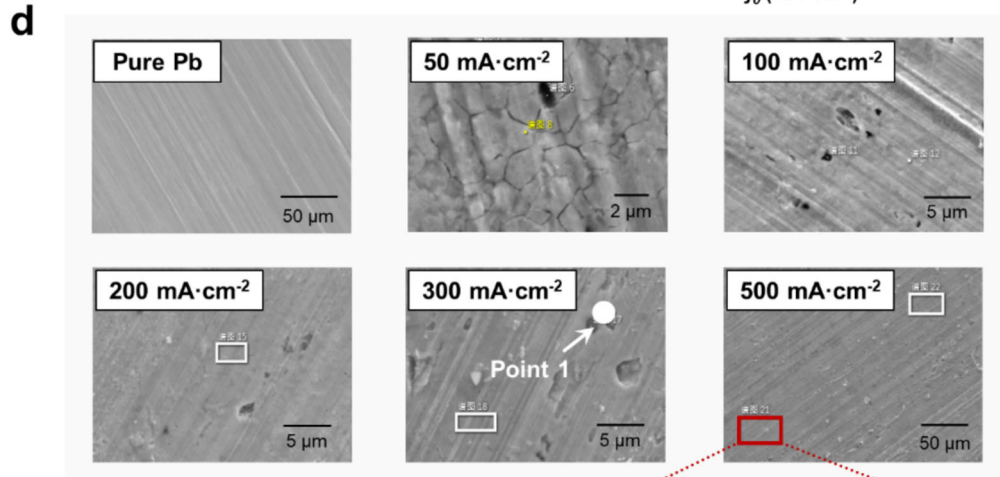
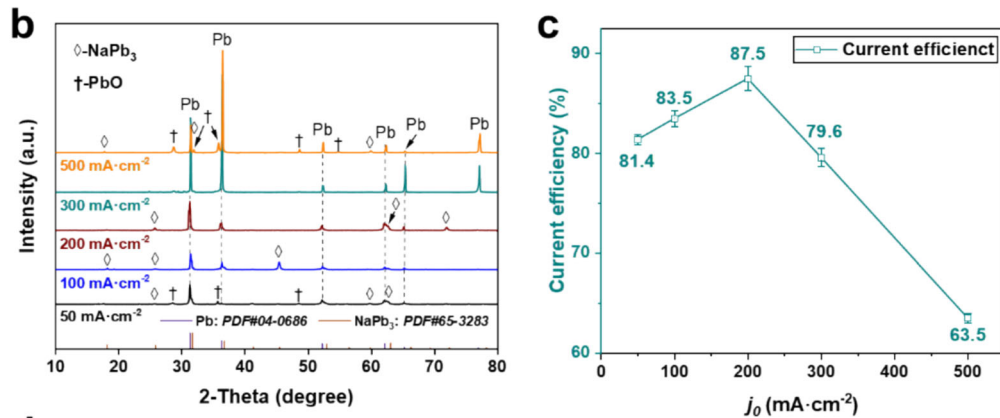
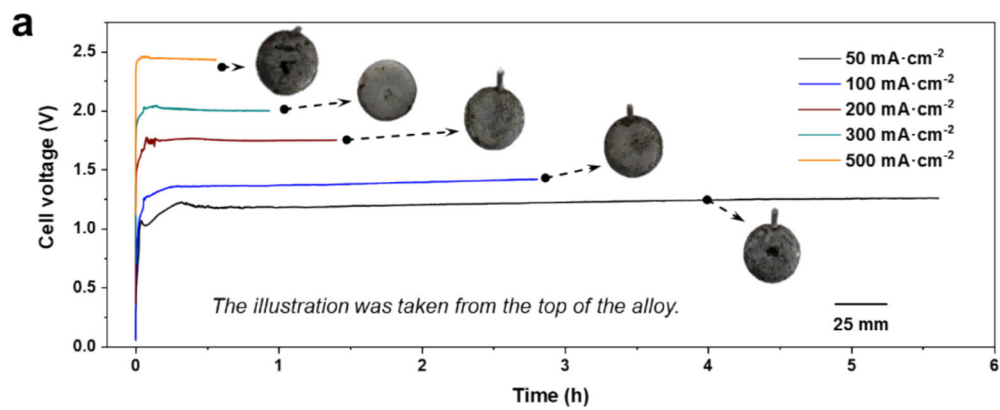


(c)

Fig. 2—(a) Schematic diagram of molten $\text{NaCl}-\text{Na}_2\text{CO}_3$ electrolysis. (b) Potential curves as a function of temperature in molten $\text{NaCl}-\text{Na}_2\text{CO}_3$, all thermodynamic data are obtained from HSC Chemistry 6.0. (c) Schematic diagram of the electrode reactions at the liquid Pb cathode and the carbon anode.

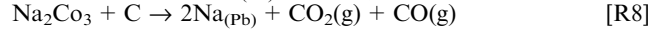
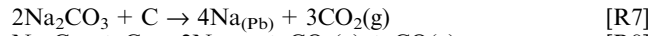
To electrochemically split Na_2CO_3 efficiently and produce Na–Pb alloys *via* a two-electrode system, a series of constant current electrolysis was conducted at 750 °C. As shown in Figure 3(a), the electrolysis cell voltage increases with the rise in current density, which is consistent with Ohm's law. Additionally, at a current density of 50 mA cm^{-2} , the electrolysis voltage remained in the range of 1.23–1.25 V, which closely matches the theoretical voltage (1.155 V). After electrolysis, the alloy surface appeared dark gray, which is attributed to the color of the passivation layer formed by the oxidation of the Na alloy [Figure 3(a)]. XRD patterns of all the alloys of weak pure Pb peaks at low current densities are likely due to the relatively poor crystallinity of Pb under such conditions [Figure 3(b)]. Analysis of the alloy samples reveals that most of the

samples ($50, 100, 200$, and 500 mA cm^{-2}) still show weak peaks for NaPb_3 , indicating that the electrolysis process effectively alloys Na with Pb. The formation of PbO in the samples is due to the passivation film formed from exposure to air during the testing process. Furthermore, the optimal electrochemical parameters can be accurately selected by measuring the Na content in the alloys and analyzing the current efficiency [Figure 3(c)]. As the current density increases, the current efficiency initially rises and then decreases, reaching a maximum of 87.5 pct at 200 mA cm^{-2} . The lower current efficiency at low current densities ($< 200 \text{ mA cm}^{-2}$) is attributed to the influence of background currents and some dissolution of Na–Pb in the electrolyte. At higher current densities ($> 200 \text{ mA cm}^{-2}$), the Na concentration on the surface



◀Fig. 3—(a) Voltage-time curves for the preparation of 2.0 wt pct Na–Pb alloy at different current densities, along with optical images of the Na–Pb alloy. (b) XRD analysis of the Na–Pb alloy. (c) Effect of current density on current efficiency. (d) SEM images and mappings of the alloy cross-section. (e) EDS surface analysis.

of the liquid Pb increases and then causes more Na to dissolve into the electrolyte. Furthermore, the higher current densities cause a negative shift in the cathode potential, resulting in carbon deposition. However, carbon is difficult to dissolve into the Na–Pb alloy, which leads to reduced current efficiency. While high current densities are unfavorable for the current efficiency of Na deposition in liquid Pb, they do not adversely affect the product. The alloy's microstructure exhibits numerous pores, which results from the high reactivity of Na–Pb alloys with air during the measurement [Figure 3(d)]. For example, Na–Pb reacts with moisture and oxygen in the air to generate hydrogen gas, leading to the formation of these pores. EDS analysis of the cross-sectional Na–Pb alloy further confirms the high reactivity of Na–Pb [Figure 3(e)]. The results show that using a liquid lead cathode and a graphite anode in molten NaCl–Na₂CO₃, Na–Pb alloys can be prepared without C deposition.^[41] Thus, the overall reaction equation in this system can be expressed as:



To investigate the effect of Na content in liquid Pb on the current efficiency, Na–Pb alloys with Na concentrations ranging from 0.5 to 3.0 wt pct were prepared by constant current electrolysis at 200 mA cm⁻². During electrolysis, the voltage was maintained at ~1.72 V, demonstrating the stability of the molten salt and confirming that the diffusion of Na⁺ ions in the molten salt and the diffusion of Na into the liquid Pb are both feasible [Figure 4(a)]. Corresponding XRD analysis confirmed the presence of NaPb₃, indicating that Na is stabilized in the form of NaPb₃ at low concentrations (< 3 wt pct Na), with its activity significantly reduced compared with pure Na [Figure 4(b)]. Further, current efficiency analysis showed that the theoretical Na content in the Na–Pb alloy should be kept below 3 wt pct, since further increasing the Na content will decrease the current efficiency lower than 80 pct [Figure 4(c)]. After electrolysis, the alloy gradually exhibited distinct crystalline phases as the Na concentration increased, which can be attributed to the embedding of Na atoms into the Pb lattice, thereby enhancing the hardness of the Na–Pb alloy [Figure 4(d)]. It was found that both Pb and Na were evenly distributed [Figure 4(e)]. This suggests that the electrochemical deposition of Na on the surface of the liquid Pb cathode is an energy-efficient and effective method.

B. Diffusion *n* of Na in Liquid Pb

In addition, the GITT method was used to measure the diffusion coefficient of Na (\tilde{D}_{Na}) in liquid Pb. The electrochemical workstation controlled the current density and charging time of the constant current pulses while measuring the equilibrium open-circuit potential changes and voltage responses during the applied current pulses. The chemical diffusion coefficient for Na in the liquid Pb of Na–Pb alloys with 0 to 20 mol pct Na during the deposition process was calculated using Eq. [2].^[42]

$$\tilde{D}_{\text{Na}} = \frac{1}{\pi} \left[\frac{2Vj_0n_{\text{Pb}} \left(\frac{\Delta E}{\Delta x_{\text{Na}}} \right)}{z_{\text{Na}}F(n_{\text{Pb}} + n_{\text{Na}}^0)^2 \frac{dE}{dt\sqrt{t}}} \right]^2, \quad [2]$$

where z_{Na} is the number of electron transfers for Na, F is the Faraday constant, n_{Na} is the moles of Na at the electrode surface (n_{Pb} corresponds to Pb), j_0 is the current density of an applied constant pulse, V is the electrode volume, E is the open-circuit potential of the Na–Pb alloy, x_{Na} is the mole percent of Na in the Na–Pb alloy, and t is the time of an applied constant pulse.

GITT tests were conducted using the parameters listed in Table I, with the results presented in Figure 5. After four constant current pulses at current densities of 50 mA cm⁻², 100 mA cm⁻², 150 mA cm⁻², and 200 mA cm⁻², the composition of Na₅Pb transformed into Na₆Pb₉₄. Similarly, after four constant pulses, the compositions of Na₁₀Pb₉₀, Na₁₅Pb₈₅, and Na₂₀Pb₈₀ transformed into Na₁₁Pb₈₉, Na₁₆Pb₈₄, and Na₂₁Pb₇₉, respectively. Following each constant pulse, the open-circuit potential (OCP) was allowed to stabilize before applying the next pulse. The ratio of the Na–Pb alloy electrode potential to the Na molar concentration was calculated (Figure 6), and the slope ($\Delta E/\Delta x_{\text{Na}}$) was determined. Additionally, the ratio of the Na–Pb alloy electrode potential to the square root of the pulse time was calculated (Figure 7), with the corresponding slope ($dE/d\sqrt{t}$) also fitted. The diffusion coefficients of Na in liquid Pb at 750 °C were calculated and are listed in Table II: 3.51 × 10⁻⁴ cm⁻² s⁻¹ (Na₅Pb₉₅), 5.11 × 10⁻⁴ cm⁻² s⁻¹ (Na₁₀Pb₉₀), 2.35 × 10⁻⁴ cm⁻² s⁻¹ (Na₁₅Pb₈₅), and 1.90 × 10⁻⁴ cm⁻² s⁻¹ (Na₂₀Pb₈₀).

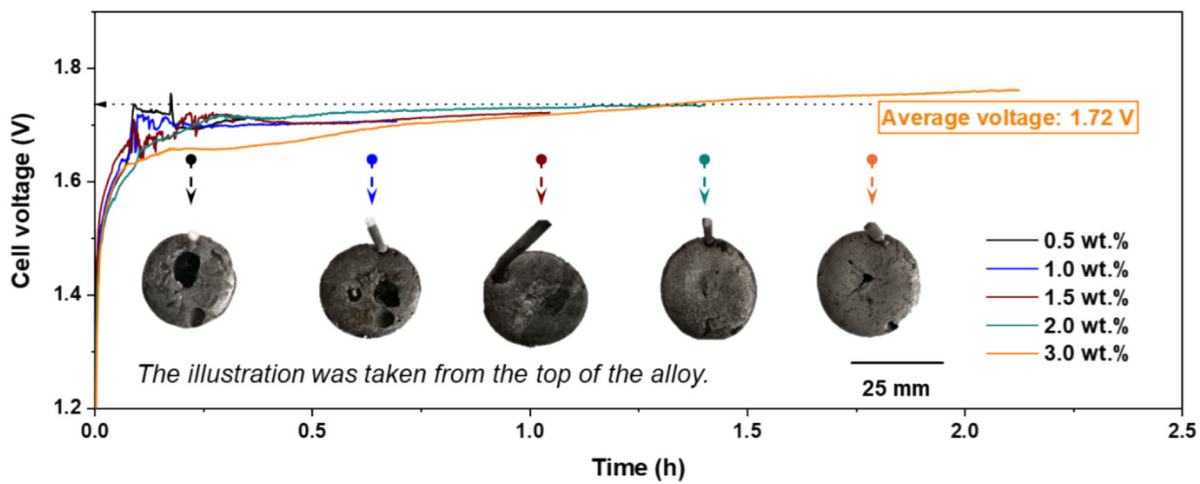
The following equation is used to describe the conservation of Na atoms in the model,

$$\frac{\partial c}{\partial t} = \nabla \cdot J = R, \quad [3]$$

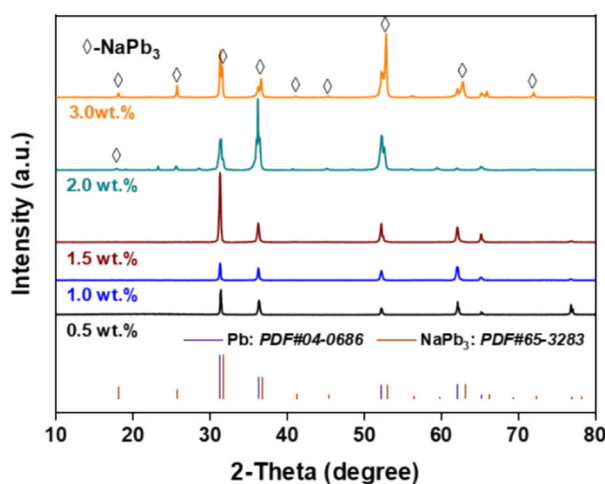
where c is the concentration of Na in a liquid Pb cathode and t is time. J is the vector of material diffusion flux. R is the amount of substances produced or reduced by the reaction of the model. J can be expressed as follows:

$$J = -D\nabla c, \quad [4]$$

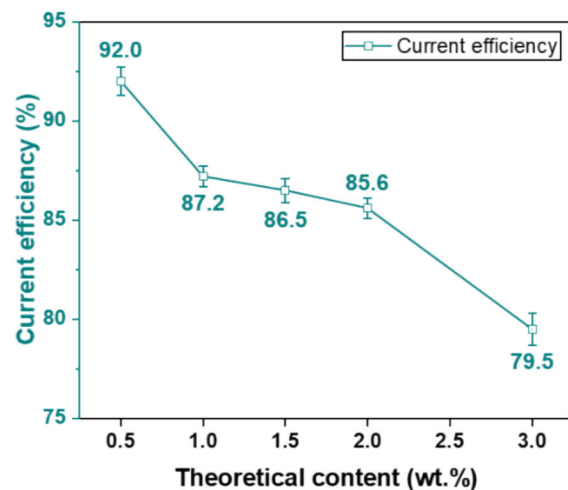
where D is the diffusion constant (i.e., $D = \tilde{D}_{\text{Na}}$, take the average value, 3.22 × 10⁻⁴ cm⁻² s⁻¹). In addition,



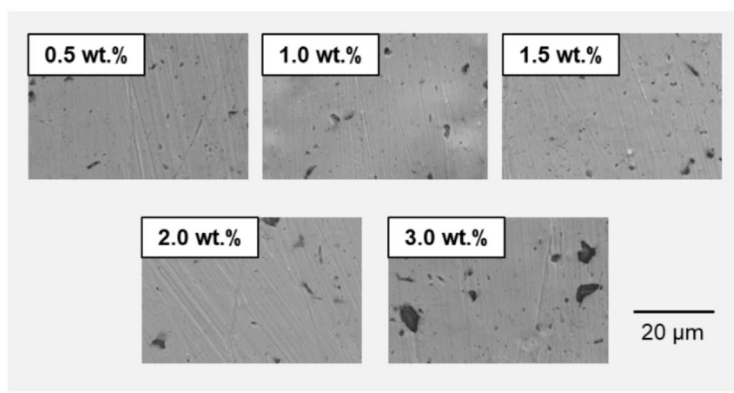
(a)



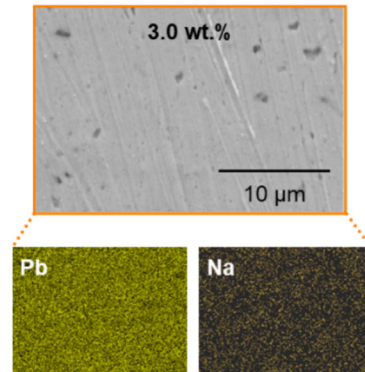
(b)



(c)



(d)



(e)

Fig. 4—(a) Voltage-time curves for the preparation of different Na-Pb alloys at 200 mA cm⁻², along with optical images of the Na-Pb alloy. (b) XRD patterns of the Na-Pb alloys. (c) Effect of current density on Na content. (d) SEM images and (e) mappings of the alloy cross-section.

Table I. Pulse Sequence Parameters of $\text{Na}_5\text{Pb}_{95}$, $\text{Na}_{10}\text{Pb}_{90}$, $\text{Na}_{15}\text{Pb}_{85}$, and $\text{Na}_{20}\text{Pb}_{80}$ Alloys

Na Molar Fraction (Pct)	Pulse (No.)	$j_0 (\text{mA cm}^{-2})$	Time (s)	ΔNa (Pct)
5.00	1	50	122.0	0.25
5.25	2	100	61.3	0.25
5.50	3	150	41.1	0.25
5.75	4	200	31.0	0.25
10.00	1	50	136.0	0.25
10.25	2	100	68.4	0.25
10.50	3	150	45.8	0.25
10.75	4	200	34.6	0.25
15.00	1	50	152.5	0.25
15.25	2	100	76.7	0.25
15.50	3	150	51.4	0.25
15.75	4	200	38.8	0.25
20.00	1	50	172.2	0.25
20.25	2	100	86.6	0.25
20.50	3	150	58.1	0.25
20.75	4	200	43.9	0.25

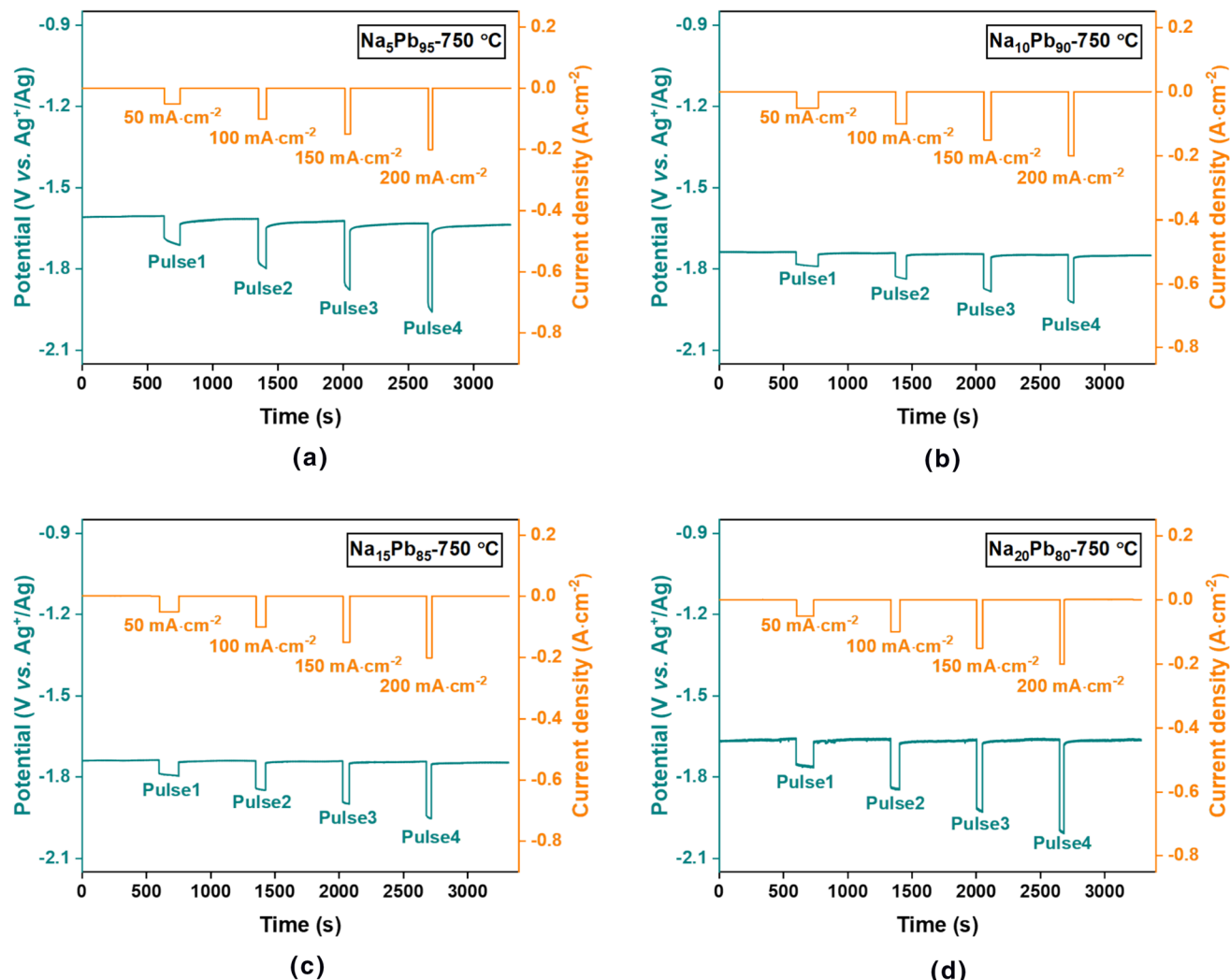


Fig. 5—Variation in current and potential (vs. RE) of (a) $\text{Na}_5\text{Pb}_{95}$, (b) $\text{Na}_{10}\text{Pb}_{90}$, (c) $\text{Na}_{15}\text{Pb}_{85}$, and (d) $\text{Na}_{20}\text{Pb}_{80}$ alloys during galvanostatic intermittent titration technique (GITT) measurements.

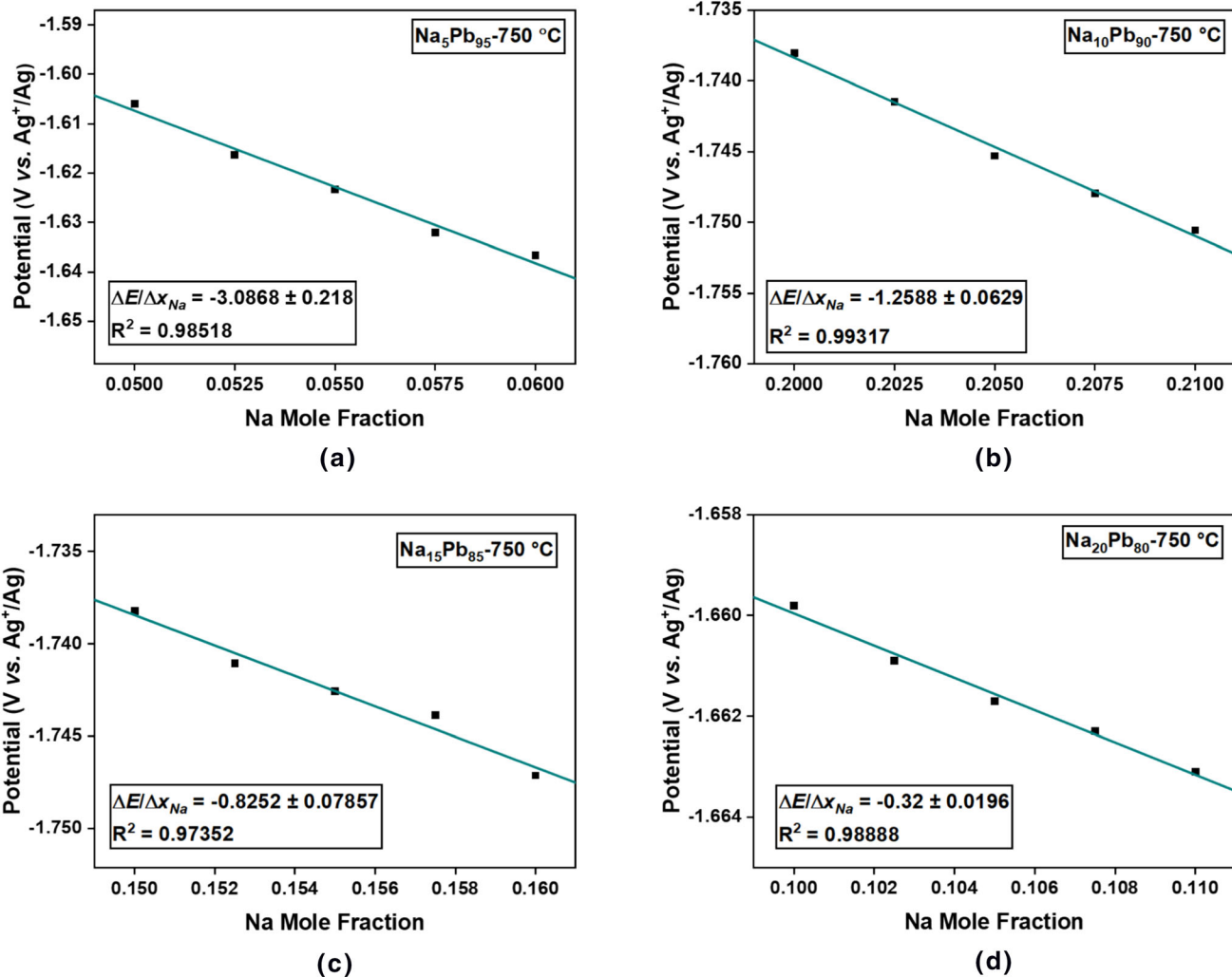


Fig. 6—Potential/molar concentration ratio ($\Delta E/\Delta x_{Na}$) of (a) Na_5Pb_{95} , (b) $Na_{10}Pb_{90}$, (c) $Na_{15}Pb_{85}$, and (d) $Na_{20}Pb_{80}$ alloys from the GITT measurements.

R can be expressed as follows:

$$R = \frac{v i_{loc}}{nF}, \quad [5]$$

where v is the stoichiometric coefficient, n is the number of electrons involved in the reaction, F is the Faraday constant, and i_{loc} is the local current density.

This model is based on the assumption that $Na_{10}Pb_{90}$ forms at the interface, with Na diffusion rates corresponding to different current densities. The Na distribution results, simulated using COMSOL 5.5, are shown in Figures 8(a) through (d). At a low current density ($< 100 \text{ mA cm}^{-2}$), the electrodeposited Na is uniformly distributed within the liquid Pb cathode. As the current density increases to 200 mA cm^{-2} , Na becomes enriched on the surface of the liquid Pb cathode, forming high-Na Na–Pb alloy phases, such as Na_4Pb . Despite the significant surface enrichment, the Na distribution within the bulk liquid Pb remains uniform. This suggests that Na can rapidly diffuse within the liquid Pb at an

optimal current density (200 mA cm^{-2}), ensuring efficient electrolysis. These results are in agreement with the experimental data.

C. Scaled Electrolyzer for the Preparation of Na–Pb Master and Grid Alloys

In a 100 A-scale electrolyzer, maintaining a stable voltage is essential to ensure electrolyte stability and prevent Cl_2 -evolution. As shown in Figures 9(a) and (b), a liquid Pb cathode of 20 kg (area: 314 cm^2) was placed at the bottom of the SS crucible, and three graphite rods (diameter: 6 mm) were used as the anodes. The electrolyte was molten $NaCl-Na_2CO_3$, and Ar gas was used as the protective gas for constant voltage electrolysis to prepare Na–Pb alloys. The voltage–current density relationship was tested before performing constant voltage electrolysis [Figure 9(c)]. As the voltage increased from 2.0 to 4.0 V, the current rose from 14 to 117 A. To achieve rapid electrolysis, constant voltage electrolysis was conducted at 4.0 V (current density:

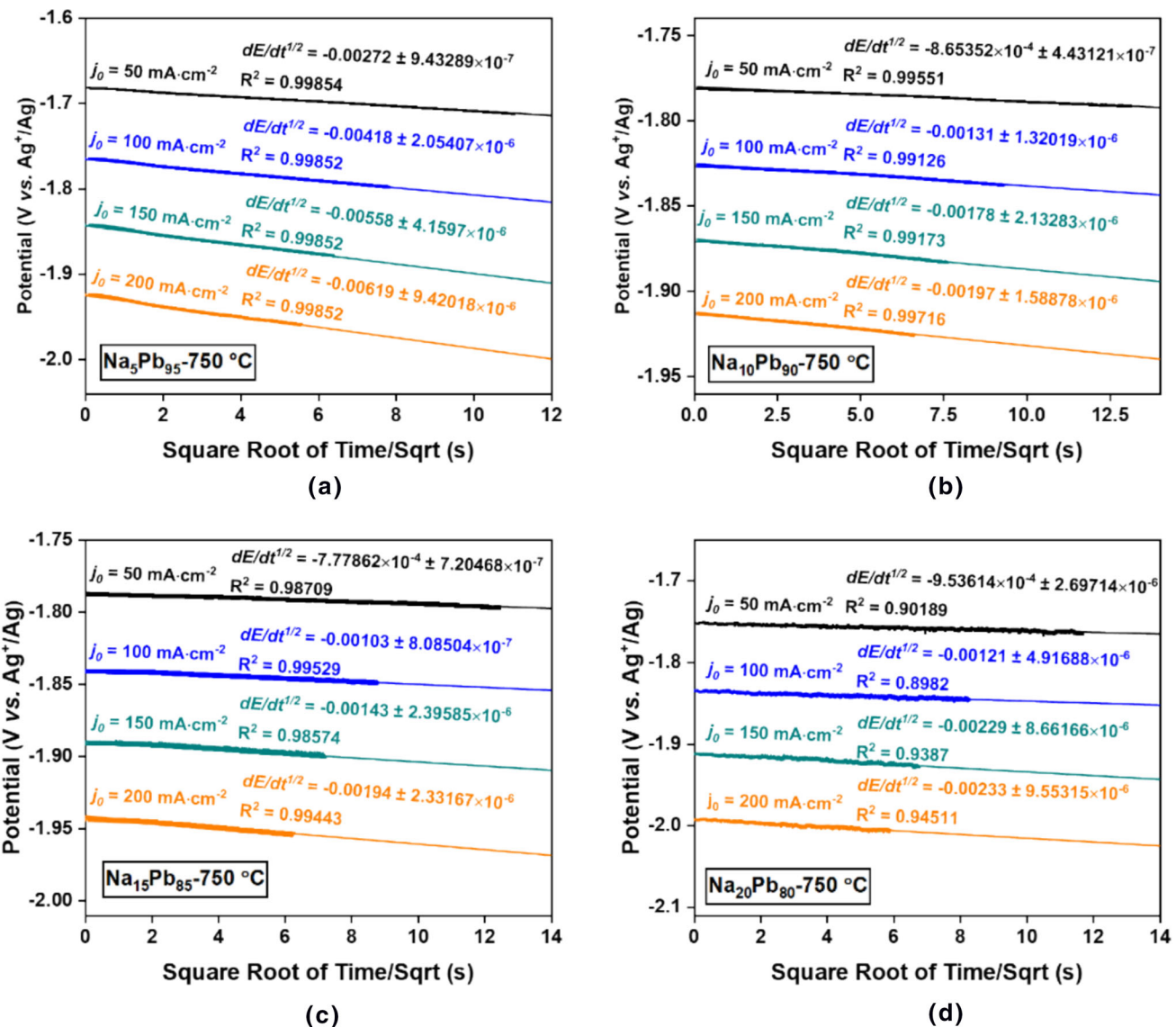


Fig. 7—Potential/Square root of time ratio ($dE/d\sqrt{t}$) of (a) $\text{Na}_5\text{Pb}_{95}$, (b) $\text{Na}_{10}\text{Pb}_{90}$, (c) $\text{Na}_{15}\text{Pb}_{85}$, and (d) $\text{Na}_{20}\text{Pb}_{80}$ alloys from the GITT measurements.

$\sim 300 \text{ mA cm}^{-2}$). The current gradually decreased over time, as the reduction potential of Na on the Pb electrode shifted negatively during the electrolysis, which is consistent with the principle of liquid metal batteries. After continuous electrolysis, the diameter of the graphite anode decreased from 40 mm to 36 mm [Figure 9(d)], confirming that the graphite anode is a consumable anode that produces $\text{CO}_2(\text{g})$ rather than $\text{Cl}_2(\text{g})$. While CO_2 is often regarded as lacking direct commercial value, its potential can be significantly enhanced when combined with CO_2 capture and electrochemical reduction technologies.^[43] By integrating CO_2 capture with electrochemical reduction, CO_2 can be converted into valuable products, such as high-performance carbon materials.^[44] The electrochemical conversion of CO_2 not only offers a sustainable method for recycling CO_2 emissions but also provides a way to generate high-value materials that can contribute to

various industrial processes. This integrated approach helps mitigate climate change by reducing CO_2 emissions while simultaneously creating valuable Na-Pb alloy products, thereby supporting the transition toward a circular economy.

After charging 1080 Ah under constant voltage electrolysis at 4.0 V, a Na-Pb alloy weighing 20.35 kg was successfully produced, as shown in the optical photograph in Figure 9(e). With the subsequent supplementation of Na_2CO_3 into the electrolyte, continuous production of Na-Pb alloys can be achieved. ICP-OES analysis revealed that the Na content in the alloy was approximately 3.52 wt pct, and the current efficiency was 76.0 pct [Figure 9(f)]. Based on these data, the cost of producing 1 ton of Na-Pb alloy with 2 wt pct Na is approximately 100.3 \$ (Table III). This represents a reduction of over 59.7 US \$ in production costs compared to the traditional method. Therefore, the

Table II. Chemical Diffusion Coefficient of Na in Liquid Na–Pb Alloys

Na–Pb Alloy Composition	No.	$\frac{\Delta E}{\Delta \chi_{\text{Na}}}$ (V)	$\frac{dE}{d\sqrt{i}}$ (V s $^{-1/2}$)	\tilde{D}_{Na} (cm 2 s $^{-1}$)
Na ₅ Pb ₉₅	1	−3.0868 ± 0.218	−0.00272 ± 9.43289 × 10 $^{-7}$	1.78544 × 10 $^{-4}$ ± 5.79204 × 10 $^{-6}$
	2	−3.0868 ± 0.218	−0.00418 ± 2.0541 × 10 $^{-6}$	3.01086 × 10 $^{-4}$ ± 9.68038 × 10 $^{-6}$
	3	−3.0868 ± 0.218	−0.00558 ± 4.1597 × 10 $^{-6}$	3.78708 × 10 $^{-4}$ ± 1.19838 × 10 $^{-5}$
	4	−3.0868 ± 0.218	−0.00619 ± 9.4202 × 10 $^{-6}$	5.44998 × 10 $^{-4}$ ± 1.64004 × 10 $^{-5}$
Na ₁₀ Pb ₉₀	1	−1.2588 ± 0.0629	−0.00087 ± 4.43121 × 10 $^{-7}$	2.59023 × 10 $^{-4}$ ± 2.83615 × 10 $^{-5}$
	2	−1.2588 ± 0.0629	−0.00131 ± 1.32019 × 10 $^{-6}$	4.50213 × 10 $^{-4}$ ± 4.88545 × 10 $^{-5}$
	3	−1.2588 ± 0.0629	−0.00178 ± 2.13283 × 10 $^{-6}$	5.46088 × 10 $^{-4}$ ± 5.90528 × 10 $^{-5}$
	4	−1.2588 ± 0.0629	−0.00197 ± 1.58878 × 10 $^{-6}$	7.89394 × 10 $^{-4}$ ± 8.59746 × 10 $^{-5}$
Na ₁₅ Pb ₈₅	1	0.8252 ± 0.07857	−0.00078 ± 7.20468 × 10 $^{-7}$	1.03007 × 10 $^{-4}$ ± 1.96230 × 10 $^{-5}$
	2	0.8252 ± 0.07857	−0.00103 ± 8.08504 × 10 $^{-7}$	2.54926 × 10 $^{-4}$ ± 2.35184 × 10 $^{-5}$
	3	0.8252 ± 0.07857	−0.00143 ± 2.3959 × 10 $^{-6}$	2.96304 × 10 $^{-4}$ ± 2.78589 × 10 $^{-5}$
	4	0.8252 ± 0.07857	−0.00194 ± 2.33167 × 10 $^{-6}$	2.84906 × 10 $^{-4}$ ± 2.65198 × 10 $^{-5}$
Na ₂₀ Pb ₈₀	1	−0.32 ± 0.0196	−0.00095 ± 2.96714 × 10 $^{-6}$	9.90132 × 10 $^{-6}$ ± 6.49291 × 10 $^{-7}$
	2	−0.32 ± 0.0196	−0.00121 ± 4.91688 × 10 $^{-6}$	2.44415 × 10 $^{-5}$ ± 1.64911 × 10 $^{-5}$
	3	−0.32 ± 0.0196	−0.00229 ± 8.66166 × 10 $^{-6}$	1.53053 × 10 $^{-5}$ ± 1.02413 × 10 $^{-5}$
	4	−0.32 ± 0.0196	−0.00233 ± 9.55315 × 10 $^{-6}$	2.61574 × 10 $^{-5}$ ± 1.76679 × 10 $^{-5}$

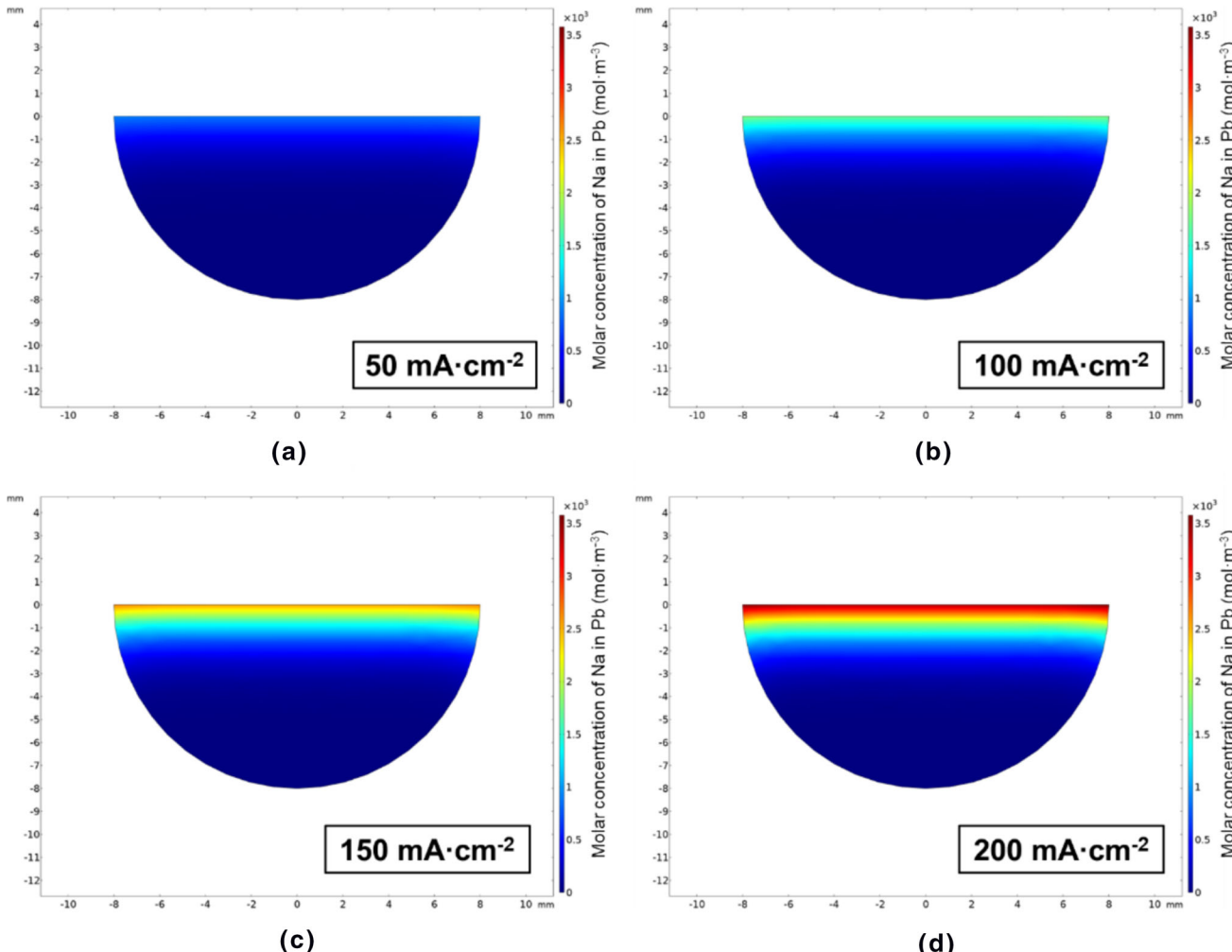


Fig. 8—Molar concentration distribution of Na in a Pb cathode when the surface is saturated during constant current electrolysis at (a) 50 mA cm $^{-2}$, (b) 100 mA cm $^{-2}$, (c) 150 mA cm $^{-2}$, and (d) 200 mA cm $^{-2}$ at 750 °C.

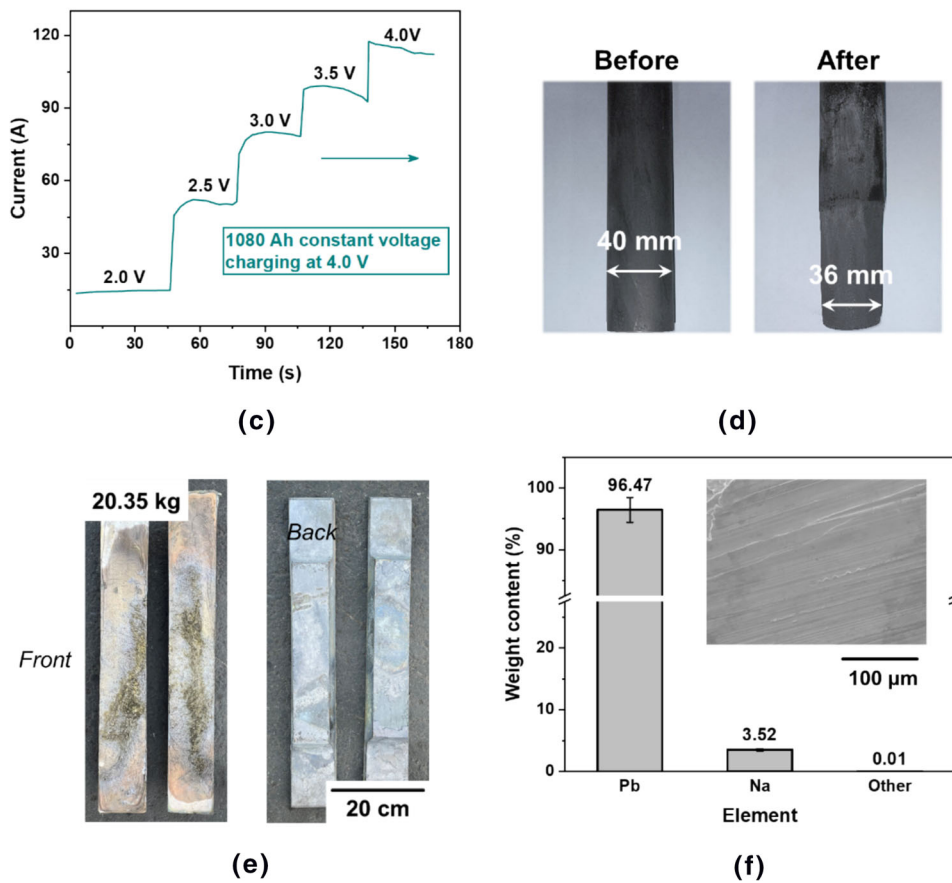
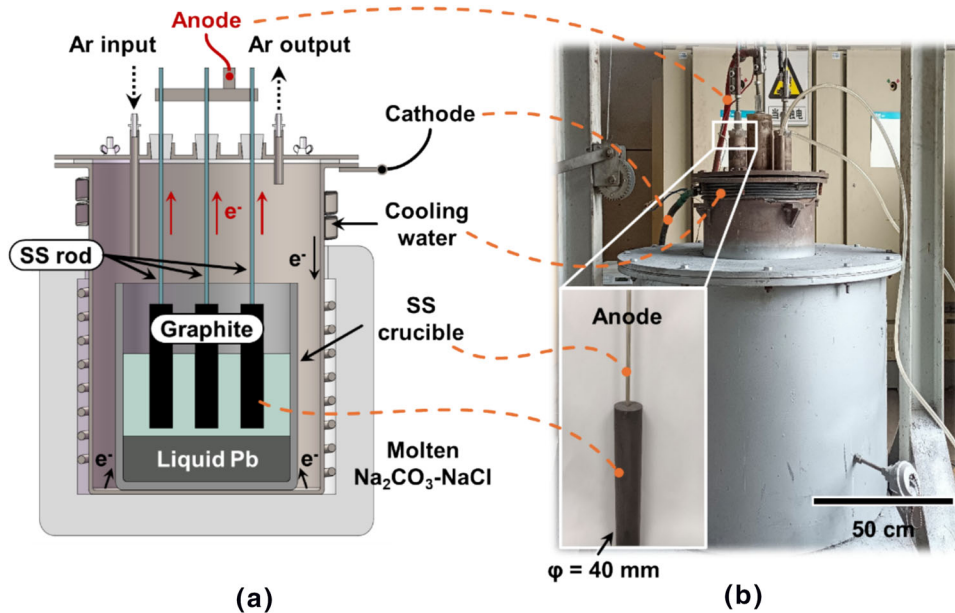


Fig. 9—(a) Schematic illustration and (b) optical images of the 100 A-scale electrolyzer to produce Na–Pb alloy production. (c) Current-time curve was recorded under different voltages from 2.0 to 4.0 V at 750 °C. (d) The graphite anode before and after electrolysis of 30 h. (e) Electrolytic Na–Pb alloy solidified in the iron vessel. (f) Elements composition analysis..

successful validation of the 100 A-scale electrolyzer demonstrates that the industrial-scale production of Na–Pb alloys is not only feasible but also cost-effective and sustainable.

To verify the suitability of the pilot-scale alloy, we fabricated Pb alloys into grid alloys to investigate the effect of Na on the mechanical properties of Pb–Ca alloys [Figure 10(a)]. Pb–Ca alloys are typically used in the current grids of sealed valve-regulated LABs. During

Table III. Comparison of the Cost for Preparing 1000 kg of Na–Pb Alloy: Traditional Method vs. This Work (Data Source: Chilwee Power)

Approach	Traditional Method	This Work
Output	1000 kg 2 wt pct Na–Pb alloy	
Input	20 kg Na (46 \$)	46.1 kg Na_2CO_3 (9.5 \$)
	980 kg Pb	980 kg Pb
	smelting cost (~114 \$)	2.6 kg C (14.9 \$)
	—	electrolysis (18.9 \$)
	—	electrolytic cell (~ 57 \$)
	160 \$	100.3 \$

Bold indicates the comparison of production costs between the traditional method and this process.

charging and discharging, significant molar volume changes occur due to the conversion between PbSO_4 and PbO_2 ($48 \text{ cm}^3 \text{ mol}^{-1}$ for PbSO_4 and $25 \text{ cm}^3 \text{ mol}^{-1}$ for PbO_2).^[45] These volume changes induce substantial material stress in the Pb-based current collectors, highlighting the importance of studying the influence of Na on the mechanical properties of Pb–Ca alloys. Figure 10(b) compares the aging hardness of Pb–Ca alloys with different Na contents after reducing the Ca content. The results show that, even with decreased Ca content, the addition of Na significantly increases hardness, with enhancements of 22.1, 24.6, and 27.3 pct, respectively. Additionally, for alloys with the same Ca content, the aging hardness increases as the Na concentration rises. As shown in Figure 10(c), the addition of Na improves the creep strength of Pb–Ca alloys and extends the creep plateau. The creep resistance increases with increasing the Na content, showing improvements of 15.2, 17.0, and 25.4 pct. Moreover, the creep strain values decrease with increasing the Na content, ranging from 0.20 for the Pb–Ca alloy to 0.32, 0.29, and 0.27, respectively. In summary, the incorporation of Na enhances both the hardness and creep

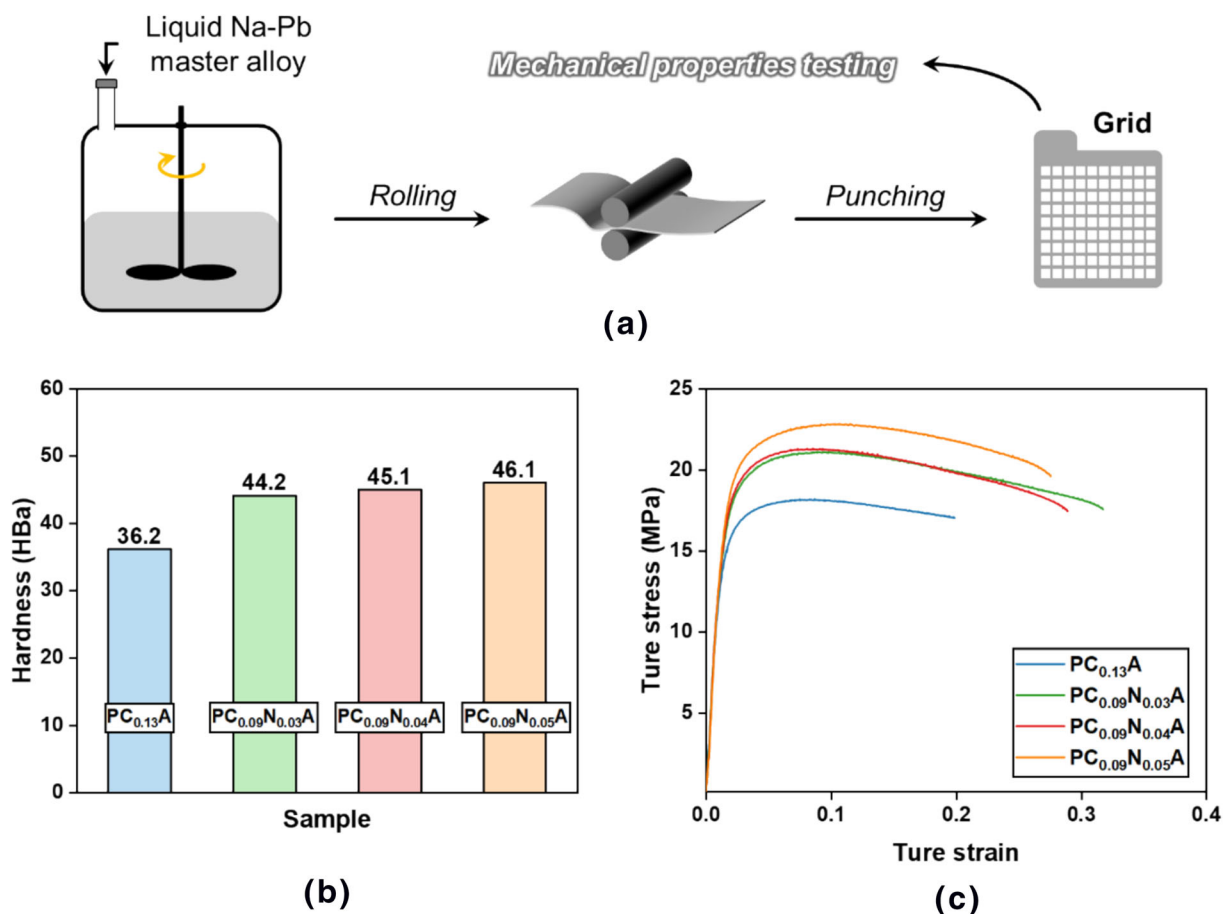


Fig. 10—(a) Production flow diagram of the lead-acid battery grid alloys. (b) Hardness and (c) creep resistance curves of $\text{Pb}-0.13\text{Ca}-0.015\text{Al}$ ($\text{PC}_{0.13}\text{A}$), $\text{Pb}-0.09\text{Ca}-0.03\text{Na}-0.015\text{Al}$ ($\text{PC}_{0.09}\text{N}_{0.03}\text{A}$), $\text{Pb}-0.09\text{Ca}-0.04\text{Na}-0.015\text{Al}$ ($\text{PC}_{0.09}\text{N}_{0.04}\text{A}$), $\text{Pb}-0.09\text{Ca}-0.05\text{Na}-0.015\text{Al}$ ($\text{PC}_{0.09}\text{N}_{0.05}\text{A}$) alloys..

resistance of Pb–Ca grid alloys, effectively mitigating issues related to deformation and fracture caused by volume changes during cycling.^[16]

IV. CONCLUSIONS

Liquid Na–Pb master (1 to 4 wt pct) alloys were directly prepared by molten salt electrolysis using a liquid Pb cathode, a NaCl–Na₂CO₃ molten salt, and a graphite anode without generating Cl₂ gas at 750 °C. The CO₃²⁻ prevented the discharge of Cl⁻ at the anode and the liquid Pb kept the generated Na–Pb at the bottom of the electrolytic cell. The current efficiency reached above 75 pct from a lab-scale cell (50 g of Pb for each cell) to a pilot cell (20 kg of Pb for each cell). The estimated cost of producing 1 ton of Na–Pb alloy is around 100.3 \$, which is lower than the current method. The diffusion coefficient of Na in liquid Pb was $3.22 \times 10^{-4} \text{ cm}^2 \text{ s}^{-1}$, indicating that the electrolysis can be performed under 200 mA cm⁻² without generating pure Na at the surface. The adding the Na–Pb master alloy in the Pb–Ca grid alloy can increase the hardness from 36.2 to 46.1 HBa and the creep resistance from 0.20 to 0.32. Therefore, Na is a good candidate for the design of grid alloys for LABs, and molten salt electrolysis holds the promise for the clean production of various Pb master alloys for high-performance LABs and other AEM-containing liquid alloys.

ACKNOWLEDGMENTS

We are grateful for the financial support from the National Natural Science Foundation of China (52374308), the Chilwee Group (CWDY-ZH-Y-JY-202101-001), the starting funding from Wuhan University, and the Fundamental Research Funds for the Central Universities (2042023kf0214).

AUTHOR CONTRIBUTIONS

Yongxin Wu: methodology, formal analysis, writing—original draft, investigation, visualization. Hongya Wang: conceptualization, writing—review & editing, supervision. Mengli Xiang, Zuojun Hu, Hao Shi, Fangzhao Pang, and Bingbing Wang: investigation, writing—review & editing. Xiong Zhang: conceptualization. Dihua Wang: writing—review & editing. Xiaowei Liu & Huayi Yin: conceptualization, resources, writing—review & editing, supervision.

DATA AVAILABILITY

Data will be made available on request.

CONFLICT OF INTEREST

The author declares that the research was conducted in the absence of any commercial or financial relation-

ships that could be construed as a potential conflict of interest.

REFERENCES

1. P.P. Lopes and V.R. Stamenkovic: *Science*, 2020, vol. 369, pp. 923–24.
2. T.P. Nguyen, A.D. Easley, N. Kang, S. Khan, S.-M. Lim, Y.H. Rezenom, S. Wang, D.K. Tran, J. Fan, R.A. Letteri, LuSu. Xun He, Yu. Cheng-Han, J.L. Lutkenhaus, and K.L. Wooley: *Nature*, 2021, vol. 593, pp. 61–66.
3. G. Deysher, Oh. Jin An Sam, Y.-T. Chen, B. Sayahpour, S.-Y. Ham, D. Cheng, P. Ridley, A. Cronk, S.-H. Lin, K. Qian, L.H.B. Nguyen, J. Jang, and Y.S. Meng: *Nat. Energy*, 2024, vol. 9, pp. 1161–72.
4. L. Ye, M. Liao, K. Zhang, M. Zheng, Yi. Jiang, X. Cheng, C. Wang, Xu. Qiuchen, C. Tang, P. Li, Y. Wen, Xu. Yifei, X. Sun, P. Chen, H. Sun, Y. Gao, Ye. Zhang, B. Wang, Lu. Jun, H. Zhou, Y. Wang, Y. Xia, Xu. Xin, and H. Peng: *Nature*, 2024, vol. 626, pp. 313–18.
5. H. Li, S. Li, R. Hou, Y. Rao, S. Guo, Z. Chang, and H. Zhou: *Chem. Soc. Rev.*, 2024, vol. 53, pp. 7742–83.
6. F. Wang, Hu. Chen, M. Zhou, K. Wang, J. Lian, J. Yan, S. Cheng, and K. Jiang: *Sci. Bull.*, 2016, vol. 61, pp. 451–58.
7. R. Shapira, G.D. Nessim, T. Zimrin, and D. Aurbach: *Energy Environ. Sci.*, 2013, vol. 6, pp. 587–94.
8. Hu. Yuchen, J. Yang, Hu. Jingping, J. Wang, S. Liang, XuWu. Huijie Hou, B. Liu, Yu. Wenhao, X. He, and R. Vasant Kumar: *Adv. Funct. Mater.*, 2018, vol. 28, p. 1705294.
9. P. Kurzweil: *J. Power. Sources*, 2010, vol. 195, pp. 4424–34.
10. Mordor intelligence: lead acid battery research, 2024. <https://www.mordorintelligence.com/industry-reports/stationary-lead-acid-battery-market>.
11. M.B. Queiroz, R.C.O. Duarte, J.F. Lima, and E.O. Vilar: *J. Power. Sources*, 2024, vol. 596, p. 234113.
12. D. Liu, Wu. Yupeng, N. Lin, Y. Wang, Z. Liu, J. Li, Q. You, J. Yin, W. Zhang, Xu. Jijing, and H. Lin: *J. Energy Storage*, 2024, vol. 101, p. 113877.
13. Wu. Yongxin, M. Cai, H. Wang, Hu. Zuojun, F. Pang, X. Chen, M. Zhao, B. Wang, X. Zhang, X. Liu, D. Wang, and H. Yin: *J. Electrochem. Soc.*, 2023, vol. 170, p. 122505.
14. M.T. Wall, Y. Ren, T. Hesterberg, T. Ellis, and M.L. Young: *J. Energy Storage*, 2022, vol. 55, p. 105569.
15. Lu. Tianliang Zhao, Y.F. Zhao, Q. Luo, J. Zhong, and Q. Li: *Corros. Commun.*, 2023, vol. 12, pp. 46–57.
16. F. Pang, Wu. Yongxin, X. Liu, X. Chen, L. Guo, S. Gao, Du. Kaifa, D. Wang, and H. Yin: *J. Energy Storage*, 2024, vol. 85, p. 110909.
17. B. Yang, X. Cai, E. Li, S. Yang, W. Liu, C. Dai, and G. Yin: *J. Energy Storage*, 2019, vol. 25, p. 100908.
18. H. Yin, B. Chung, F. Chen, T. Ouchi, Ji. Zhao, N. Tanaka, and D.R. Sadoway: *Nat. Energy*, 2018, vol. 3, pp. 127–31.
19. S. Zhang, Ye. Liu, Q. Fan, C. Zhang, T. Zhou, K. Kalantar-Zadeh, and Z. Guo: *Energy Environ. Sci.*, 2021, vol. 14, pp. 4177–4202.
20. H. Kim, D.A. Boysen, J.M. Newhouse, B.L. Spatocco, B. Chung, P.J. Burke, D.J. Bradwell, K. Jiang, A.A. Tomaszowska, K. Wang, W. Wei, L.A. Ortiz, S.A. Barriga, S.M. Poizeau, and D.R. Sadoway: *Chem. Rev.*, 2013, vol. 113, pp. 2075–99.
21. K. Wang, K. Jiang, B. Chung, T. Ouchi, P.J. Burke, D.A. Boysen, D.J. Bradwell, H. Kim, U. Muecke, and D.R. Sadoway: *Nature*, 2014, vol. 514, pp. 348–50.
22. L. Tang, A. Li, H. Chen, He. Li, Q. Chen, H. Zhou, W. Wei, W. Zhang, Hu. Jie, C. Dou, H. Wang, and D. Finlow: *Electrochim. Acta*, 2011, vol. 56, pp. 4566–70.
23. D.K.J. Lee, Z. Deng, G.S. Gautam, and P. Canepa: *Chem. Mater.*, 2024, vol. 36, pp. 6831–37.
24. R.A. Khairulin, S.V. Stankus, R.N. Abdullaev, and V.A. Morozov: *J. Phase Equilib. Diffus.*, 2012, vol. 33, pp. 369–74.
25. N.W. Gregory: *Chem. Educ.*, 1957, vol. 34, p. 103.
26. R. Cao, K. Mishra, X. Li, J. Qian, M.H. Engelhard, M.E. Bowden, K.S. Han, K.T. Mueller, W.A. Henderson, and J.-G. Zhang: *Nano Energy*, 2016, vol. 30, pp. 825–30.

27. C. Dierk Raabe, C. Tasan, and E.A. Olivetti: *Nature*, 2019, vol. 575, pp. 64–74.
28. N. Johnson and P. Albertus: *J. Electrochem. Soc.*, 2022, vol. 169, p. 060546.
29. A. Kafle, D. Gupta, S. Mehta, K. Garg, and T.C. Nagaiah: *J. Mater. Chem. A*, 2024, vol. 12A, pp. 5626–41.
30. P. Govier and J.M. Coulson: *Toxicol. Lett.*, 2018, vol. 293, pp. 249–52.
31. Z. Li, L. Zhu, H. Liu, Y. Lin, D. Tang, L. Zhou, Y. Dai, Z. Gao, F. He, K. Guo, Yu. Neng, and Z. Liu: *Sep. Purif. Technol.*, 2023, vol. 313, p. 123477.
32. H. Jiao, S. Jiao, W.-L. Song, H. Chen, M. Wang, Tu. Jiguo, and D. Fang: *J. Electrochem. Soc.*, 2019, vol. 166, p. E401.
33. R. Song, X. Wang, S. Luo, C. Jiang, and D. Tang: *Mater. Sci.*, 1996, vol. 6, pp. 18–25.
34. M. Kamaludeen, K. Balakrishnan, and G. Singh: *Bull. Electrochem.*, 1990, vol. 6, pp. 107–108.
35. L. Guo, S. Gao, Hu. Zuojun, Wu. Yongxin, F. Pang, H. Yin, and D. Wang: *Green Chem.*, 2024, vol. 26, pp. 2763–72.
36. L. Guo, H. Yin, W. Li, S. Wang, K. Du, H. Shi, X. Wang, and D. Wang: *J. Magnes. Alloys*, 2024.
37. H. Yin, B. Deng, Du. Kaifa, W. Li, S. Gao, H. Shi, and D. Wang: *Chin. Sci. Bull.*, 2023, vol. 68, pp. 3998–4014.
38. H. Shi, Z. Fang, M. Cai, M. Liu, P. Wang, Du. Kaifa, H. Yin, and D. Wang: *ACS Sustain. Chem. Eng.*, 2023, vol. 11, pp. 9235–42.
39. H. Shi, P. Li, Z. Yang, K. Zheng, Du. Kaifa, L. Guo, Yu. Rui, P. Wang, H. Yin, and D. Wang: *ACS Sustain. Chem. Eng.*, 2022, vol. 10, pp. 13661–68.
40. H. Zhou, H. Li, Q. Gong, S. Yan, X. Zhou, S. Liang, W. Ding, Y. He, K. Jiang, and K. Wang: *Energy Storage Mater.*, 2022, vol. 50, pp. 572–79.
41. Hu. Xiaofei, P.H. Joo, E. Matios, C. Wang, J. Luo, K. Yang, and W. Li: *Nano Lett.*, 2020, vol. 20, pp. 3620–26.
42. L. Guo, H. Yin, S. Gao, S. Wang, Du. Kaifa, H. Shi, and D. Wang: *Metall. Mater. Trans. B*, 2024, vol. 55B, pp. 128–43.
43. T. O'Carroll, X. Yang, K.J. Gordon, L. Fei, and Wu. Gang: *Adv. Energy Mater.*, 2024, vol. 14, p. 2401558.
44. B. Deng, H. Yin, Du. Kaifa, and D. Wang: *Sci. Chin. Chem.*, 2023, vol. 66, pp. 3116–35.
45. X. Ma, S. Zhou, J. Cao, Y. Yang, Z. Chen, Yi. Liu, S. Zhou, and B. Jiang: *J. Energy Storage*, 2024, vol. 84, p. 110710.

Publisher's Note Springer Nature remains neutral with regard to jurisdictional claims in published maps and institutional affiliations.

Springer Nature or its licensor (e.g. a society or other partner) holds exclusive rights to this article under a publishing agreement with the author(s) or other rightsholder(s); author self-archiving of the accepted manuscript version of this article is solely governed by the terms of such publishing agreement and applicable law.